IJMMM International Journal of Minerals, Metallurgy and Materials 矿物冶金与材料学报（英文版）

Two-stage dynamic recrystallization and texture evolution in Al–7Mg alloy during hot torsion

Kwang Tae Son, Chang Hee Cho, Myoung Gyun Kim, and Ji Woon Lee

Cite this article as:
Kwang Tae Son, Chang Hee Cho, Myoung Gyun Kim, and Ji Woon Lee, Two-stage dynamic recrystallization and texture evolution in Al–7Mg alloy during hot torsion, *Int. J. Miner. Metall. Mater.*, 31(2024), No. 8, pp. 1900-1911. https://doi.org/10.1007/s12613-024-2877-9

INTERNATIONAL JOURNAL OF
Minerals, Metallurgy and Materials

Volume 31, Number 8, August 2024
Page 1900

Research Article https://doi.org/10.1007/s12613-024-2877-9

Two-stage dynamic recrystallization and texture evolution in Al–7Mg alloy during hot torsion

Kwang Tae Son[1)], *Chang Hee Cho*[2)], *Myoung Gyun Kim*[3)], *and Ji Woon Lee*[4,5),✉]

1) School of Mechanical, Industrial, and Manufacturing Engineering, Oregon State University, Corvallis OR 97331, USA
2) Department of Materials Science Engineering, Northwestern University, Evanston IL 60208, USA
3) Research Institute of Industrial Science and Technology (RIST), Pohang 37673, Rep. of Korea
4) Division of Advanced Materials Engineering, Kongju National University, Cheonan 31080, Rep. of Korea
5) Center for Advanced Materials and Parts of Powders, Kongju National University, Cheonan 31080, Rep. of Korea
(Received: 8 January 2024; revised: 18 February 2024; accepted: 7 March 2024)

Abstract: Hot torsion tests were performed on the Al–7Mg alloy at the temperature ranging from 300 to 500°C and strain rates between 0.05 and 5 s^{-1} to explore the progressive dynamic recrystallization (DRX) and texture behaviors. The DRX behavior of the alloy manifested two distinct stages: Stage 1 at strain of ≤2 and Stage 2 at strains of ≥2. In Stage 1, there was a slight increase in the DRXed grain fraction (X_{DRX}) with predominance of discontinuous DRX (DDRX), followed by a modest change in X_{DRX} until the transition to Stage 2. Stage 2 was marked by an accelerated rate of DRX, culminating in a substantial final X_{DRX} of ~0.9. Electron backscattered diffraction (EBSD) analysis on a sample in Stage 2 revealed that continuous DRX (CDRX) predominantly occurred within the $(1\bar{2}1)$ [001] grains, whereas the (111) [110] grains underwent a geometric DRX (GDRX) evolution without a noticeable sub-grain structure. Furthermore, a modified Avrami's DRX kinetics model was utilized to predict the microstructural refinement in the Al–7Mg alloy during the DRX evolution. Although this kinetics model did not accurately capture the DDRX behavior in Stage 1, it effectively simulated the DRX rate in Stage 2. The texture index was employed to assess the evolution of the texture isotropy during hot-torsion test, demonstrating significant improvement (>75%) in texture randomness before the commencement of Stage 2. This initial texture evolution is attributed to the rotation of parent grains and the substructure evolution, rather than to an increase in X_{DRX}.

Keywords: Al–7Mg alloys; hot deformation; hot torsion tests; dynamic recrystazlliation; microstructure; texture

1. Introduction

Dynamic recrystallization (DRX) plays a pivotal role in industrial thermomechanical processes such as rolling, forging, and extrusion for metallic materials [1–3]. By contributing to grain refinement and reducing deformation resistance, DRX mechanisms become crucial factors in determining optimal processing conditions [4]. Moreover, a fine-grained structure offers significant advantages by retarding material failure through the suppression of uneven deformation and void formation [5]. In the realm of hot deformation of metallic materials, three primary DRX mechanisms have been identified [6]. Discontinuous DRX (DDRX), one such mechanism, typically occurs near grain boundaries and expands by incorporating the adjacent deformed regions. This process exhibits spatial and temporal heterogeneity within the material matrix, reflecting a predilection for specific locations. Another mechanism, continuous DRX (CDRX), involves the continuous rotation of cells or sub-grains during deformation, facilitated by the cumulative reorganization of dislocations. This reorganization leads to an increase in the misorientation angles between sub-grains and their environs. Geometric DRX (GDRX), bearing resemblance to CDRX but without distinct nucleation events, activates at large strains. It segments large grains into smaller equiaxed ones through grain boundary impingement and localized lattice rotation. It is broadly recognized that CDRX, or GDRX, predominates as the chief DRX mechanism under conditions of low strain rates or elevated temperatures [7].

Generally, Al alloys are commonly known to exhibit a dominant dynamic recovery (DRV) mechanism due to its high stacking fault energy (SFE) of 160–250 mJ/m² [8–9]. From a perspective suggested by Galindo-Nava *et al*. [10], the DRV frequency decreases with a decrease in alloy density and the volume of the dislocation annihilating, achieved by adding more Mg in Al–Mg alloys. In contrast, an increase in Mg levels can expedite the frequency of DDRX with restricted grain boundary migration and a large solute-drag effect due to higher solute content [11]. This indicates that the addition of Mg to Al alloys has the potential to shift the dominant DRX mechanism from CDRX or GDRX to DDRX. This intriguing aspect has prompted extensive research on the

✉ Corresponding author: Ji Woon Lee E-mail: jwl@kongju.ac.kr

DRX behavior of Al–Mg alloys over several decades. Most studies have concluded that the restoration mechanism in Al–Mg alloys is governed by GDRX. Some researchers examined deformed microstructures of Al–Mg alloys with Mg content up to 5.8wt%, which exhibited typical GDRX characteristics with cumulative misorientation increase of subgrains from early strains (ε = 1, 2) to large strains (ε = 10.8) [12–13]. However, a recent study revealed that higher Mg additions to Al alloys (8wt% and 9wt%) resulted in a transition of the main DRX mechanism towards DDRX in Al–Mg alloys [14]. Therefore, investigating the DRX mechanism of the Al–7Mg alloy will help bridge the gap between low Mg-containing (≤6wt%) and high Mg-containing (≥8wt%) binary Al–Mg alloys.

DRX is anticipated to significantly enhance the formability of Al alloys by promoting grain size uniformity and the development of equiaxed grain morphology. Beyond influencing these basic grain shape characteristics, recrystallization plays a pivotal role in altering the crystal orientation, or texture, of the material [15], a critical property that impacts mechanical behaviors. In Al–Mg alloys, the emergence of a copper-type texture (comprising copper, brass, and S orientations) has been shown to adversely affect formability [16–17]. Conversely, a random texture in Al alloys has been found to prevent earing formation [18], with the achievement of uniform deformation from such a texture improving planar anisotropy and thereby reducing the risk of fracture during metal forming processes [19]. Nonetheless, this random texture may not always yield the optimal formability across various strain modes due to the lack of geometrical hardening [20]. While there has been extensive research on the texture of cold-worked and annealed alloys, the evolution of hot deformation texture in Al–Mg alloys, especially concerning DRX and at large strains, has been less frequently reported. A study on the Al–3Mg alloy revealed that at elevated temperatures and reduced strain rates, texture randomness increased up to relatively minor strains ($\varepsilon \leq 0.6$) [21], a phenomenon believed to afford enhanced formability with mechanical isotropy [22]. However, the texture evolution in Al–Mg alloys with high Mg content and subjected to large strains, potentially involving GDRX, remains a largely unexplored domain. Thus, exploring the texture evolution alongside DRX in Al–7Mg alloys during hot deformation up to significant strain levels presents a worthwhile investigation.

This study is to investigate the progressive DRX and texture behaviors during the hot deformation of Al–7Mg alloy, with a specific focus on strains larger than those typically achieved in tension or compression tests (typically $\varepsilon \leq 2$). It reveals how variations in deformation parameters influence the transition between different DRX mechanisms, offering critical insights into optimizing processing conditions for improved microstructural control and mechanical properties in Al–Mg systems. To achieve the stated objective, the hot-torsion test was selected for its ability to apply large strains while simultaneously recording the stress–strain curve, which is not shared by other severe plastic deformation methods such as equal channel angular pressing and high-pressure torsion [6]. Furthermore, this mode of simple shear deformation, offering access to large strains, proves more advantageous for structural modification through grain size refinement compared to the pure shear mode [23]. Observations of microstructure and texture in the hot-torsioned Al–Mg alloys were carried out to gather data on DRX and texture evolution. In addition, DRX kinetics were analyzed using a modified Avrami's equation. The primary goal behind deriving DRX kinetics was to predict microstructural refinement facilitated by DRX, utilizing the stress–strain curve as a basis, thereby minimizing reliance on direct microstructure observations alone.

2. Experimental

A torsion test was employed in this study to investigate the DRX and texture behaviors of Al–7Mg alloy during hot deformation. The hot extruded Al–7Mg alloy rods, with an extrusion ratio of 25.3:1, were provided by the Korea Institute of Industrial Technology. The alloy was consisted of Mg 6.93wt%, Mn 0.74wt%, Fe 0.09wt%, Si 0.06wt%, Zn 0.04wt%, Ca 0.08wt%, and Al. For the torsion tests, samples with a gauge length of 20 mm and a radius of 5 mm were machined. Prior to the torsion tests, the samples were annealed in air at 530°C for 3 h.

Torsion tests were conducted in the temperature range of 300 to 500°C, with strain rates ranging from 0.05 to 5 s^{-1}. The samples were heated at a rate of 1°C/s and held at the test temperatures for 600 s. The tests were continued until sample failure occurred or were interrupted at a specific strain for microstructure observation. To preserve the microstructure developed during the tests, the samples were water-quenched within a few seconds after the torsion tests. The effective stress (σ) and effective strain (ε) were calculated using the Von Mises criterion and the method of Fields and Backofen [24].

Deformed microstructures were observed on a tangential plane of the samples. The samples were cut parallel to the torsion axis at a distance of 0.7r (r represents sample radius). A graphical illustration of this sample observation is available elsewhere [25]. Microstructure observation was performed by optical microscopy (OM), electron backscatter diffraction (EBSD), and transmission electron microscopy (TEM). OM was used to observe the grains of the sample before/after deformation. The samples for OM were anodized in a solution of 10% H_3PO_4 in distilled water at 50°C using a Struers Lectropol 5 machine. EBSD was performed on 300 μm × 300 μm area with a step size of 0.5 μm to determine the sub-grain structures and misorientation angles (θ). A Hitachi 4300SE scanning electron microscope equipped with an EDAX EBSD camera was used for the EBSD data collection. The DRX volume fraction of the samples was measured using grain orientation spread mapping in EBSD. Generally, a grain orientation spread (GOS) value of less than 2°, combined with a relatively smaller grain size of less than 8 μm, indicates regions where recrystallization has occurred

[26–27]. Three deformation conditions were selected for the characterization of DRX and texture evolution: 300°C, 0.05 s^{-1}; 400°C, 0.05 s^{-1}; 500°C, 0.5 s^{-1}. The choice of 500°C, 0.5 s^{-1} instead of 500°C, 0.05 s^{-1} was decided because the DRX kinetics derivation was not available for the latter condition, as discussed later.

EBSD was also used to plot the shear texture volume fraction of the hot-torsioned samples. For the texture identification, a deviation of ≤15° from the ideal orientation was applied. Table 1 lists the ideal shear texture components according to Bunge's notation. The samples for EBSD were prepared by electropolishing with a solution of 20% perchloric acid in methanol at −30°C using a Struers Lectropol 5 machine. TEM observations were conducted using a Jeol JEM-2100F machine. Samples for TEM observations were prepared using a Struers TenuPol-5 twin-jet polisher.

Table 1. Ideal shear texture components of FCC materials (Bunge notation, given in Euler angle of $g = (\varphi_1, \Phi,$ and $\varphi_2)$)

Orientation	Shear plane	Shear direction	φ_1 / (°)	Φ / (°)	φ_2 / (°)
A	$(11\bar{1})$	$[1\bar{1}0]$	0	35.26	45
$\bar{A}$	$(\bar{1}\bar{1}1)$	$[\bar{1}10]$	180	35.26	45
A_1^*	$(11\bar{1})$	$[2\bar{1}1]$	35.26	45	0
A_2^*	$(1\bar{1}1)$	$[\bar{2}\bar{1}1]$	144.74	45	0
B	$(11\bar{2})$	$[1\bar{1}0]$	0	54.74	45
$\bar{B}$	$(\bar{1}\bar{1}2)$	$[\bar{1}10]$	180	54.74	45
C	(100)	$[0\bar{1}1]$	90	45	0

Table 2. Experimental data of Al–7Mg obtained from effective stress–strain curves

T / °C	$\dot{\varepsilon}$ / s^{-1}	σ_p / MPa	ε_p	σ_{ss} / MPa	ε_{ss}	ε_f	ln$Z$
300	0.05	190.36	0.31	—	—	2.37	33.07
	0.5	225.28	0.34	—	—	1.58	35.37
	5	249.22	0.30	—	—	0.81	37.67
400	0.05	115.74	0.06	68.81	4.89	8.55	27.71
	0.5	147.46	0.17	—	—	2.91	30.01
	5	184.93	0.26	—	—	1.70	32.31
500	0.05	59.692	0.01	32.92	4.01	9.20	23.74
	0.5	87.83	0.04	53.04	4.52	7.66	26.04
	5	120.17	0.14	—	—	1.93	28.34

Note: T is temperature, $\dot{\varepsilon}$ is strain rate, σ_p is peak stress, ε_p is peak strain, σ_{ss} is steady-state stress, ε_{ss} is strain where the steady-state initiates, ε_f is strain at fracture, and ln$Z$ is natural logarithm of the Zener–Hollomon parameter.

3. Results

3.1. Flow curves

Fig. 1 presents flow curves of the Al–7Mg alloy obtained from hot torsion tests at different temperatures (300 to 500°C) and strain rates (0.05 to 5 s^{-1}). Table 2 provides the corresponding mechanical properties, including peak stress (σ_p) and fracture strain (ε_f). The flow curves exhibit initial strain hardening, consistent with typical metal deformation behavior. Decreasing temperature and increasing strain rate lead to higher peak stress and peak strain (ε_p). Conversely, higher temperatures and lower strain rates result in increased fracture strain, indicating improved hot ductility. All flow curves show a distinct peak stress, indicating the occurrence of DRX. Beyond the peak stress, flow softening occurs as strain continues, indicating the initiation of dynamic microstructural development. This flow softening leads to a steady state, where the microstructure becomes stable, featuring a dense DRX structure.

In general, the relationship between the flow stress and the deformation conditions, such as temperature and strain rate, is expressed through the Zener–Hollomon (Z) parameter [2]. It has also been reported that this single processing parameter can effectively be used for studying DRX in metals, replacing the need for multiple processing parameters such as temperature and strain rate [6]. In this study, the constitutive equation was established using the hyperbolic sine law, as follows:

$$Z = \dot{\varepsilon} \exp[Q/(RT)] = 7.99 \times 10^{12} \times [\sinh(0.0067\sigma_p)]^{10.8} \quad (1)$$

where Z, $\dot{\varepsilon}$, Q, R, T, and σ_p are the Zener–Hollomon parameter, the strain rate, the activation energy for hot working, the gas constant (8.3145 $J \cdot K^{-1} \cdot mol^{-1}$), the temperature, and the peak stress, respectively. The activation energy for hot working, Q, was calculated to be 171.8 $kJ \cdot mol^{-1}$. This activation energy is somewhat higher than the self-diffusion energy of Al atoms in the Al matrix (≈142 $kJ \cdot mol^{-1}$). It has been reported that Q increases with the addition of more solute atoms to the Al matrix as these solute atoms act as obstacles to dislocation movement [28–29]. Jeong *et al.* [30] reported a comparable activation energy (Q) value of 179.8 $kJ \cdot mol^{-1}$ for Al–7Mg under hot compression within the same temperature range but at a different strain rate range of 5×10^{-4} to 10 s^{-1}. This indicates a minor discrepancy in the activation energy

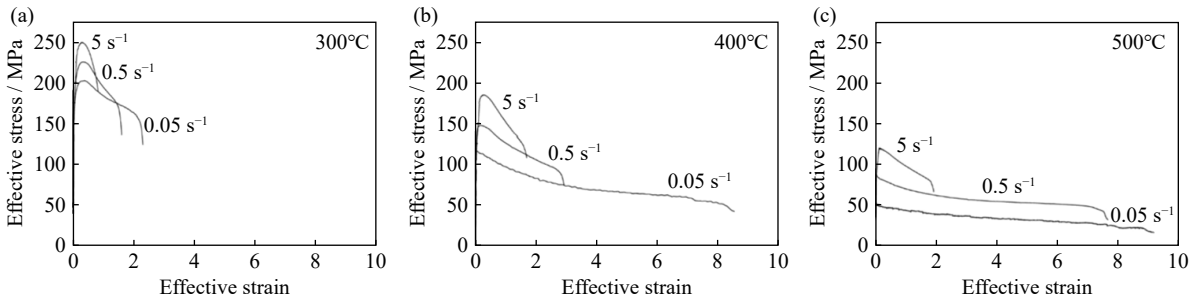

Fig. 1. Flow curves of Al–7Mg deformed at (a) 300°C, (b) 400°C, and (c) 500°C under the strain rates of 0.05, 0.5, and 5 s^{-1}.

due to differences in conditions. Calculations of the activation energy based on Eq. (1) for three different deformation modes [31] also support this viewpoint, showing approximately 5 $kJ \cdot mol^{-1}$ difference in Q values across three different deformation modes for the same Al alloy, temperature, and strain rates. At high Z values, which correspond to faster strain rates or lower temperatures, the flow curves showed moderate strain hardening followed by flow softening up to the point of fracture. Conversely, at low Z parameters, indicative of slower strain rates or higher temperatures, there was a rapid increase in flow stresses, with flow softening advancing to a steady-state, with the exception being the outcome at 500°C and strain rate of 5 s^{-1}.

The detailed analysis of Fig. 1 uncovers two distinct profiles in the flow curves under varying deformation conditions: (i) gradual increase in stress followed by broad peak and (ii) swift escalation in stress culminating in sharp peak. Flow curves exhibiting the type (i) peak typically occur under high Z conditions, associated with lower temperatures and higher strain rates. Conversely, flow curves displaying the type (ii) peak are predominantly found under low Z conditions, indicative of environments where DRV is prevalent.

3.2. Deformed/undeformed DRX microstructure observation using EBSD

Fig. 2 displays EBSD images of the Al–7Mg alloy before and after undergoing hot torsion tests. The colored regions in the figure signify the occurrence of DRX. As depicted in Fig. 2(a), none of the grains in the undeformed structure fulfill the criteria for DRX, characterized by grain orientation spread (GOS) value of less than 2° and grain size smaller than 8 μm. This observation confirms that all the colored grains in the deformed structures (Fig. 2(b)–(d)) have undergone DRX. Essentially, the undeformed structure, with a minimum grain size of 8 μm, sets the threshold for identifying DRXed grains in the study of DRX using EBSD data.

At the lowest temperature of 300°C, a reduced amount of DRX was observed, characterized by flow curves with a broad peak without reaching a steady-state. In this scenario, DRX predominantly occurred along the grain boundaries of parent grains, accompanied by localized DRX within shear bands, identifying these grains as undergoing CDRX within shear bands [6]. The shear banding effect narrowed the grain boundaries, thereby accelerating lattice rotation and the occurrence of CDRX. A comparison between the two lower strain conditions depicted in Fig. 2(c)–(d) shows that the

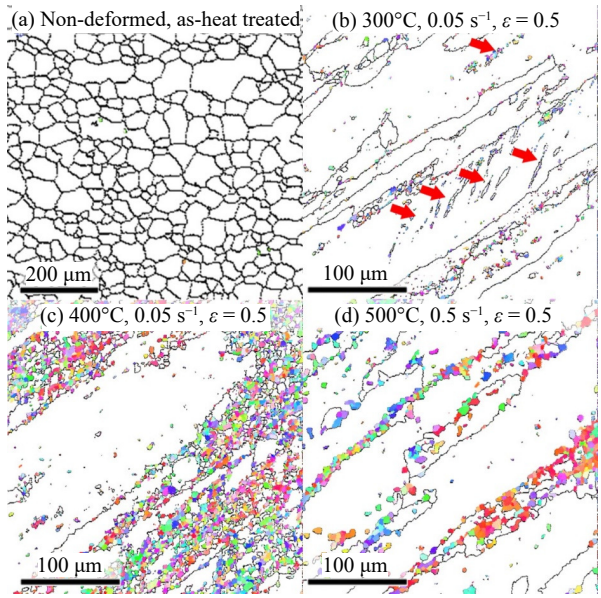

Fig. 2. DRX area visualization using criterion of GOS < 2° and grain size smaller than 8 μm: (a) non-deformed, as heat-treated sample; deformed samples up to $\varepsilon = 0.5$ in torsion conditions at (b) 300°C, 0.05 s^{-1}, (c) 400°C, 0.05 s^{-1}, and (d) 500°C, 0.5 s^{-1}. In the images, black lines represent grain boundaries with θ greater than 15°, and the DRX area is indicated by color. The red arrows in (b) indicate where shear-bands were formed.

sample at 400°C demonstrated a higher DRX fraction than the one at 500°C for strain of 0.5. This lower DRX fraction at the reduced temperature can be ascribed to the more active DRV at elevated temperatures, as previously mentioned. This assertion is supported by the calculated geometrical necessary dislocation density (GND), with the 500°C sample exhibiting a lower GND level of $(7.1 \pm 7.2 \times 10^{13})$ m^{-2}, in contrast to the 400°C sample, which presented a higher GND value of $(9.9 \pm 10.1 \times 10^{13})$ m^{-2}. A lower GND at identical strain levels indicates a faster DRV rate or increased dislocation annihilation.

To delve deeper into the progressive DRX behavior in the Al–7Mg alloy during hot torsion, the condition of 400°C and 0.05 s^{-1}, which showed the largest DRX fraction at the same strain, was chosen for further investigation. Multiple EBSD datasets were collected across continuous strains, as illustrated in Fig. 3. At smaller strains (≤3), both elongated parent grains and small equiaxed grains formed through DRX are evident. The proportion of equiaxed grains gradually rises with strain, yet a fully recrystallized structure remains un-

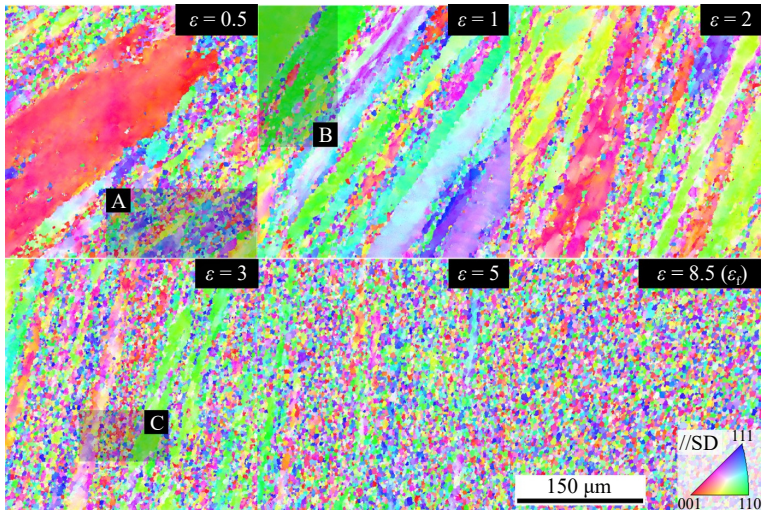

Fig. 3. Inverse pole figure (IPF) maps of Al–7Mg alloy deformed at 400°C under a strain rate of 0.05 s^{-1} at the various deformation strains. The shear direction (SD) is indicated as vertical in the images. The color of the grain orientation corresponds to the shear direction, as illustrated by the orientation triangle located at the bottom-right corner. The scale of individual images in Fig. 3 is the same. Section A, B, and C are the specific areas for further analyses in discussion section.

Table 3. DRXed grain size evolution during hot torsion

Deformation condition	300°C, 0.05 s^{-1}, ln$Z$ = 33.07			400°C, 0.05 s^{-1}, ln$Z$ = 27.71						500°C, 0.5 s^{-1}, ln$Z$ = 26.04					
Strain	0.5	1	2.2	0.5	1	2	3	5	8.2	0.5	1	2	3	5	7.6
DRXed grain size / μm	1.42± 0.70	1.54± 0.65	1.36± 0.45	2.23± 1.29	2.31± 1.34	2.33± 1.37	2.38± 1.25	2.63± 1.37	2.80± 1.48	2.80± 2.05	2.82± 1.95	3.25± 2.13	3.69± 2.28	3.64± 2.11	3.84± 2.21

Note: The measured initial grain size before hot-torsion was (31.9 ± 15.4) μm (Fig. 2(a)).

achieved even at a strain of 5.

By a strain of 0.5, equiaxed grains are predominantly located at the boundaries of elongated grains. With increasing strain ($\varepsilon \geq 1$), an increase in DRXed grains is noted, and elongated grains begin to align with the shear direction. DRX primarily takes place near grain boundaries. At low strains ($\varepsilon < 2$) under the 400°C and 0.05 s^{-1} condition, DRX initiation is observed at the boundaries of parent grains and may extend inward. With the strain increasing to $\varepsilon = 5$, parent grains nearly align parallel to the shear direction.

Table 3 outlines the evolution of DRXed grain size in Al–7Mg alloys during hot torsion. The data highlights a trend of smaller DRXed grains at higher Z parameters of deformation. Remarkably, the size of DRXed grains consistently enlarges at lower Z conditions, specifically at 400°C, 0.05 s^{-1} and 500°C, 0.5 s^{-1}. This increase in DRXed grain size is notably more significant under the lower Z condition.

3.3. Prediction of the hot-deformed grain structure with DRX

Grain refinement can be effectively achieved through DRX during hot working. Within the DDRX mechanism, new grains form at the boundaries of parent grains, leading to the replacement of parent grains by DRXed grains once a sufficient strain is reached. The size of DDRXed grains typically remains constant up until the strain level that corresponds to the steady-state is attained [1]. However, as indicated in Table 3, the size of DRXed grains increased with strain under specific deformation conditions, likely attributable to the utilization of stored energy surrounding the DRX areas.

The DRXed grain size decreases as the temperature decreases and the strain rate increases. Generally, the DRXed grain size does not depend on the initial grain size, but rather on the deformation conditions, such as temperature and strain rate [32]. The following relationship represents the DRXed grain size of Al–7Mg as a function of the Z parameter.

$$D_{DRX} = 188.67Z^{-0.153} \quad (2)$$

where D_{DRX} is the DRXed grain size. The relationship was derived from the linear regression of the measured DRXed grain size after torsion tests with various deformation conditions. As Z is as a function of temperature and strain rate, the DRXed grain size can be predicted and controlled with the temperature and strain rate.

3.4. Deformed shear texture and texture randomness evolution during hot torsion

Generally, a grain structure that is randomly oriented or exhibits a weak texture tends to display superior isotropy in its properties. Although complete randomness of texture in a polycrystal does not invariably ensure optimal formability, it facilitates acceptable formability without the significant mechanical drawbacks associated with unfavorably textured grains [16–17]. Notably, a random texture is particularly effective in mitigating defect formation during sheet metalworking processes [18–19].

Fig. 4 illustrates the evolution of shear texture during the hot torsion of Al–7Mg alloys under three specific conditions: 300°C at 0.05 s^{-1}, 400°C at 0.05 s^{-1}, and 500°C at 0.5 s^{-1}. Samples processed at 400 and 500°C show an initial

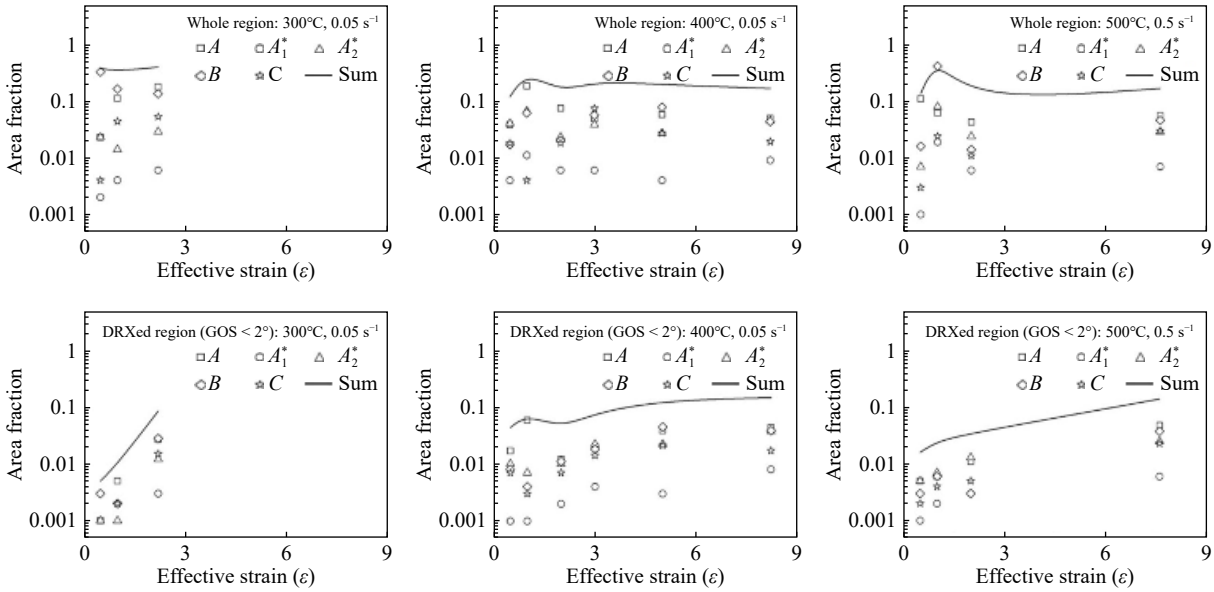

Fig. 4. Ideal shear texture evolution during hot torsion of Al–7Mg alloys under 300°C 0.05 s^{-1}, 400°C 0.05 s^{-1}, and 500°C 0.5 s^{-1}. The shear texture fraction of whole region is given in the first row and the shear texture fraction of DRXed region is given in the second row.

strengthening of shear texture at early strains ($\varepsilon < 1.5$), which subsequently weakens ($\varepsilon \approx 2.5$) until reaching a steady state ($\varepsilon \gtrapprox 3$). A higher fraction of ideal shear texture is observed under larger Z conditions. Remarkably, in areas where DRX occurred, the fractions of shear texture gradually increase until rupture, particularly under larger Z conditions. At highly DRXed states ($\varepsilon > 7$), the intensity ranking of shear components follows the order $A > B > A_2^* > C > A_1^*$. However, with the total fraction of these ideal shear textures being close to 0.1, it remains challenging to assert that a pronounced texture developed in the Al–7Mg alloy due to DRX or hot deformation within the explored temperature range of 300 to 500°C.

The texture index (TI) offers a more intuitive approach for evaluating texture randomness or material isotropy than merely calculating individual texture strengths, as depicted in Fig. 4. Defined in [33] and derivable through calculations in EBSD software, the TI provides a holistic measure of the overall texture characteristic. This allows for a more insightful analysis of texture randomness or isotropy within the material, facilitating a deeper understanding of how texture influences the mechanical properties and formability of Al–7Mg alloys.

$$\text{Texture index (TI)} = \int f(g)^2 \mathrm{d}g \tag{3}$$

where $f(g)$ is the orientation distribution function which is defined as the probability of finding a crystallite of certain orientation $g = \{\varphi_1, \Phi, \varphi_2\}$, and g is the Euler coordinate given in Table 1. The texture index (TI) represents the overall texture randomness of the material, regardless of the specific crystallite orientations where the highest intensities occur. The higher value of TI indicates more textured or more anisotropic material, while a fully random texture corresponds to TI value of unity.

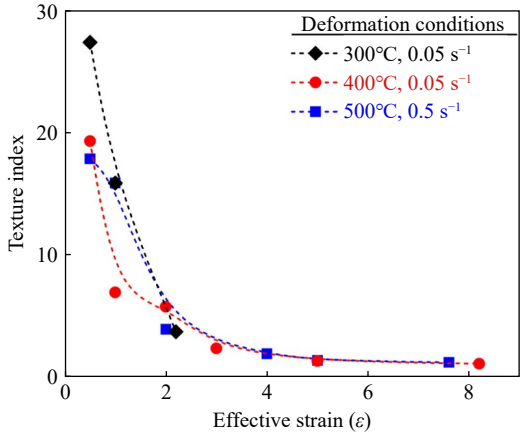

Fig. 5. Evolution of TI during hot torsion tests of Al–7Mg alloys under three different conditions. The straight green line represents TI = 1, which corresponds to the theoretical perfect random texture.

Fig. 5 illustrates the evolution of the TI in hot-torsioned Al–7Mg samples under various conditions: 500°C at 0.5 s^{-1}, 400°C at 0.05 s^{-1}, and 300°C at 0.05 s^{-1}. Initially, at $\varepsilon = 0.5$, all three samples display the highest levels of material anisotropy. Under larger Z conditions, there is a noticeable reduction in texture randomness at the early strains. However, as the strain progresses, the TI gradually declines towards unity, signaling the development of an ideally random texture or an isotropic polycrystalline structure. This decline in TI follows a non-linear trajectory, with the bulk of the reduction occurring by $\varepsilon = 2$. Remarkably, even with low volume fraction of DRX (X_{DRX}) at $\varepsilon = 2$ in the 400°C, 0.05 s^{-1} sample, there is a pronounced 70% decrease in TI from $\varepsilon = 0.5$ to $\varepsilon = 2$. This significant change suggests that DRX may not be the sole contributing factor to the randomization of texture during the hot deformation of Al–7Mg alloys.

3.5. DRX kinetics for the prediction of DRX volume fraction

The evolution of microstructure resulting from DRX dur-

Table 4. Parameters of kinetics model for DRX obtained from effective stress–strain curves of Al–7Mg alloy

T / °C	$\dot{\varepsilon}$ / s^{-1}	ε_c	ε^*	k'	m'
400	0.05	0.052	0.772	0.32	1.28
500	0.05	0.007	0.238	0.83	0.53
	0.5	0.032	0.548	0.51	0.90

ing hot deformation can be forecasted using a DRX kinetics model. Numerous models for DRX kinetics have been proposed across various materials. In our study, a modified kinetics model, inspired by Kim's model [34] and Serajzadeh's model [35], was utilized to predict changes in the extent of X_{DRX} during hot deformation. The equation employed to characterize this relationship is outlined as follows:

$$X_{DRX} = 1 - \exp\left[-k'\left(\frac{\varepsilon - \varepsilon_c}{\varepsilon^*}\right)^{m'}\right] \quad (4)$$

where ε_c is the critical strain for the initiation of DRX, ε^* is the strain required for maximum softening rate, and k' and m' are constants.

The parameters for the DRX kinetics model were derived from experimental data presented in Table 4. The work hardening rate ($n = d\sigma/d\varepsilon$) was calculated from flow curves and graphed against effective stress and strain, as shown in Fig. 6. At a strain of approximately 0.5, the n curve for the condition at 500°C, 0.05 s^{-1} reaches zero, implying the completion of DRX. However, such an implication is unlikely at this low strain level, with no preceding evidence to support the premature completion of DRX in Al alloys possessing an initial grain size larger than 30 μm. Therefore, the current DRX kinetics model does not suit the 500°C, 0.05 s^{-1} condition. Consequently, an alternative condition (500°C, 0.5 s^{-1}) was selected for analyzing the evolution of DRX volume fraction, facilitating a comparison between empirical observations and theoretical predictions.

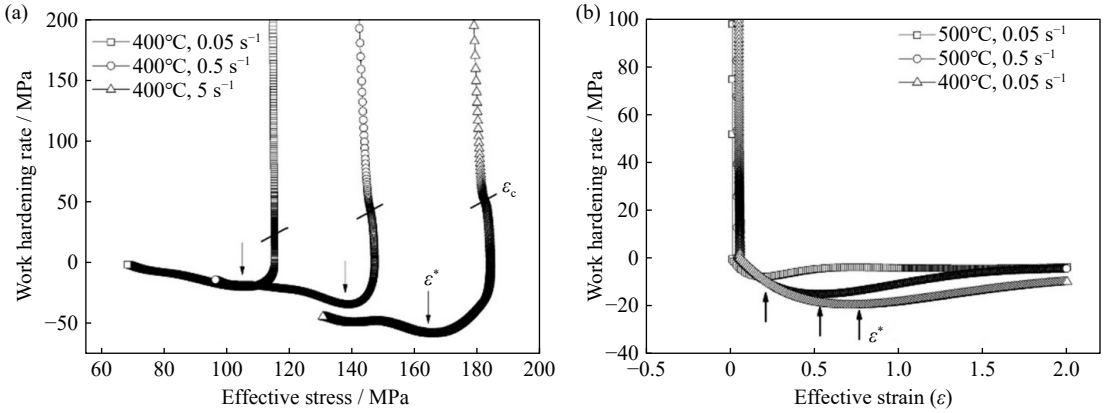

Fig. 6. (a) Work hardening rate–effective stress curves to determine the critical strain for Al–7Mg alloy and (b) work hardening rate–effective strain curves to determine the strain for maximum softening rate. The softening rate evolution of the 500°C, 0.05 s^{-1} condition is unevaluable beyond $\varepsilon \approx 0.6$, hence not available for the DRX kinetic derivation.

To determine the critical strain for the initiation of DRX (ε_c), the point where $\partial^2 n/\partial\sigma^2$ is zero was identified from Fig. 6(a) [36]. The values of ε_c increased as the temperature decreased and the strain rate increased. Additionally, the strain required for the maximum softening rate (ε^*) was determined from the n–ε relationship in Fig. 6(b). The values of ε^* increased as the temperature decreased and the strain rate increased. To determine the constants k' and m', the relationship of the fractional softening in the effective stress, which represents the fraction of DRX, was utilized [37] as follows:

$$X_{DRX} = \frac{\sigma_p - \sigma}{\sigma_p - \sigma_{ss}} \quad (5)$$

where σ_p and σ_{ss} are the peak stress and steady-state stress, respectively. By combining Eqs. (4) and (5), k' and m' were determined by linear regression.

Fig. 7 displays the kinetics curves of the Al–7Mg alloy under various deformation conditions. The X_{DRX} increases with strain, achieving 100% at larger strains (>7). X_{DRX} both initiates and completes earlier under lower Z conditions, exhibiting a slower rate beyond the DRX acceleration point. The measured X_{DRX} significantly deviates from the calculated values, with a maximum discrepancy of more than 0.46. These discrepancies are more pronounced in the condition of 500°C at 0.5 s^{-1} (lower Z) compared to the condition of 400°C at 0.05 s^{-1} (higher Z). The model does not accurately

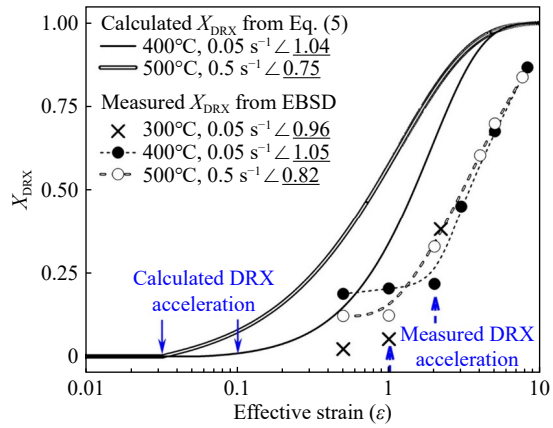

Fig. 7. Calculated and measured volume fraction of DRXed grains, based on the kinetics model for DRX (Eq. (5)) and EBSD, for Al–7Mg at various deformation conditions. Underlined and bold numbers are kinetic slopes. DRX acceleration points are different between the calculated values and measured values.

predict the early strain increase in X_{DRX} prior to DRX acceleration and forecasts DRX acceleration at lower strains, contrary to the observed data. Such inconsistencies underscore the limitations of the current DRX kinetics model in precisely predicting the DRX evolution in the Al–7Mg alloy. Nevertheless, the calculated X_{DRX} successfully mirrors the measured DRX speed, or the steepness of the kinetics slope, beyond the DRX acceleration point. This suggests that further refinement or modifications of the model are needed to enhance its predictive accuracy for specific alloy and deformation conditions, especially concerning lower strain DRX behaviors.

4. Discussion

In the hot deformation of metallic alloys, it is crucial to consider the effects of strain rate and temperature on the microstructure. The Z parameter effectively illustrates how the interplay between temperature and strain rate influences DRX mechanisms and the resulting deformation texture in Al–7Mg alloys. Conditions of low Z, corresponding to high temperatures and low strain rates, promote the development of fine-grained recrystallized structures through CDRX and GDRX, leading to a weaker deformation texture at early strains. Conversely, high Z conditions, characterized by low temperatures and high strain rates, tend to favor DDRX, resulting in stronger deformation textures at early strains. However, as evidenced in Fig. 7, the DRX behavior of hot-torsioned Al–7Mg alloys in this study cannot be solely interpreted through a single DRX mechanism, necessitating a more detailed discussion on this topic.

4.1. Progressive DRX behaviors in the Al–7Mg during hot-torsion

In Al alloys, the high SFE promotes the occurrence of cross-slip and the climb of dislocations, thereby activating DRV through dislocation annihilation and reorganization. CDRX is seen as an "extended" form of DRV, involving progressive dislocation reorganization that transforms sub-grains into grains during thermomechanical processes. CDRX has been identified as not only the predominant DRX mechanism at low strains [38] but also at very large strains [39] in the hot deformation of Al alloys. GDRX, characterized by local bulging of parent grain boundaries, represents a specific form of CDRX and is recognized as the dominant DRX mechanism in Al–Mg alloys with Mg content of ≤6wt% [12–13]. The inclusion of Mg into Al alloys significantly lowers the SFE, impeding the processes of dislocation cross-slip and climb. As a result, the principal DRX mechanism in Al–Mg alloys with a higher Mg content (≥8wt%) transitions to DDRX [14].

4.1.1. DDRX occurrence at early strains ($\varepsilon \leq 2$) before the DRX acceleration

EBSD analysis of the Al–7Mg alloy, deformed at 400°C and strain rate of 0.05 s^{-1} as illustrated in Fig. 8(a)–(b), reveals IPF maps and corresponding grain boundary maps that

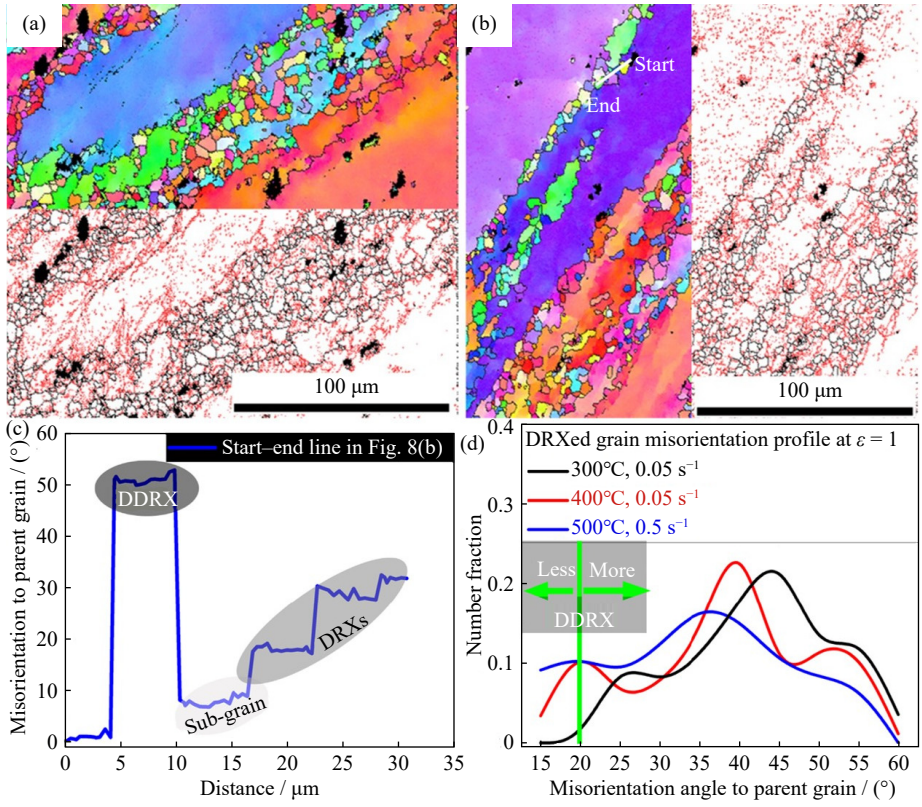

Fig. 8. IPF maps with corresponding grain boundary maps of hot-torsioned 400°C 0.05 s^{-1} sample in Fig. 3: (a) $\varepsilon = 0.5$; (b) $\varepsilon = 1$; (c) misorientation profile along the white line in (b); (d) DRXed grain misorientation profile at $\varepsilon = 1$ for three different hot-torsion conditions. Grain boundary maps in (a) and (b) consist of black lines (grain boundaries, $\theta > 15°$) and red lines (sub-grain boundaries, $\theta < 15°$). As given in the green arrows in (d), it is unlikely for CDRX to have $\theta > 20°$ at $\varepsilon = 1$ [46–47].

highlight the presence of equiaxed grains at the boundaries of elongated parent grains. These grains, exhibiting characteristics of complete DRX as observed in Fig. 2, predominantly form a "necklace" structure around the parent grains, a hallmark commonly associated with DDRX under hot deformation conditions [40]. DDRX typically begins at low strains ($\varepsilon \leq 1$), suggesting that the DRXed grains in Fig. 8(a)–(b) are likely products of DDRX, a hypothesis further corroborated by the misorientation profile in Fig. 8(c) where three out of four DRXed grains exhibit θ greater than 20° relative to the parent grain. Fig. 8(d) confirms a significant proportion of these high-misorientation DRXs relative to the parent grain.

Previous research [41–42] suggests that DDRX is characterized by higher θ values compared to CDRX, with CDRX relative to the parent grain typically showing $\theta \leq 20°$, particularly at smaller strains. Consequently, DRXed grains with $\theta \leq 20°$ in Fig. 8(c) are likely indicative of CDRX. Although the 20° threshold may not be universally applicable for differentiating DDRX from CDRX across all materials and thermomechanical conditions, it is generally accepted that CDRX is characterized by low θ values at small strains, signifying a gradual transformation from very low θ sub-grains (≤2°) [6,40]. While GDRX might present a larger θ than CDRX, due to its evolution via the impingement of parent grain boundaries, its presence at low strain levels is typically not observed, aligning with the absence of "pinched-off" parent grains in Fig. 3 for strains ≤ 2.

In Fig. 8(d), the fraction of CDRX-dominant grains (those with $\theta \leq 20°$) is higher in the lower Z condition, aligning with the general behavior of DRX in metals. However, even in these lower Z conditions, the fraction of DDRX exceeds that of CDRX, suggesting a dominance of DDRX formation at this strain level ($\varepsilon = 1$) for the lower Z condition. Considering the observation that DDRX occurs more frequently at higher Z conditions during the hot deformation of Al alloys [43], it is determined that DDRX is the main DRX mechanism for the higher Z conditions (which has total strains lower than 2) presented in Fig. 1. Furthermore, Fig. 7 shows that there is no remarkable increase in the volume fraction of DRX (XDRX) between $\varepsilon = 0.5$ and the onset of DRX acceleration ($\varepsilon \leq 2$) in all three conditions. Therefore, it is concluded that DDRX is the primary DRX mechanism at low strains ($\varepsilon \leq 2$) in the Al–7Mg alloy during hot deformation.

4.1.2. CDRX and GDRX mechanisms after the onset of DRX acceleration ($\varepsilon > 2$)

In Fig. 7, a notable increase in X_{DRX} is observed beyond the DRX acceleration point. Although DDRX typically occurs at grain boundaries during the incubation phase or before DRX acceleration, it is unlikely to account for the abrupt rise in X_{DRX}. If DDRX were the primary driver behind X_{DRX} evolution, a gradual rather than sudden increase in X_{DRX} would be anticipated. Hence, CDRX or GDRX is more likely responsible for the notable increase in X_{DRX} at larger strains ($\varepsilon > 2$). This is supported by a previous study [44] that reported a shift in recrystallization mechanisms from DDRX to CDRX at high strains, even in metals with lower SFE like Mg alloys.

CDRX and GDRX are conducive to smaller grain sizes, resulting in lower dislocation densities for substructure formation and a significant size ratio of sub-grains to the parent grain [6,40]. A minimal grain diameter along a minor axis suffices for initiating a fine-grained structure essential for CDRX or GDRX; the median grain size is less crucial in this context. Fig. 9(a) shows the variation in average grain width with strain across three hot-torsion conditions. The correlation between the X_{DRX} plot in Fig. 7 and the abrupt reduction in grain width in Fig. 9(a) suggests that decreasing grain width is essential for DRX acceleration during hot torsion of Al–7Mg. This observation leads to the speculation that CDRX or GDRX significantly contributes to the increase in X_{DRX} beyond the steady X_{DRX} region at lower strains ($\varepsilon \leq 2$).

Further analysis into this speculation involves examining substructure evolution within parent (or elongated) grains during the X_{DRX} jump phase. Fig. 9(b) reveals crystal orientation through IPF maps and sub-grain boundary distribution via a grain boundary map from EBSD analysis. Grain A is characterized by numerous sub-grains, giving it an almost fragmented appearance, in contrast to Grain B, which lacks a developed sub-grain structure. θ profiles plotted along white lines A and B in Fig. 9(b-iv), as depicted in Fig. 9(c), distinctly show that Grain A undergoes a more significant lattice rotation along the shear direction compared to Grain B. Heidarzadeh *et al*. [45] attribute a smaller increase in θ along the shear direction to GDRX, as opposed to the traditional CDRX mechanism, which involves a gradual increase in θ from sub-grain boundaries to grain boundaries. The Taylor factor map in Fig. 9(b-iv) corroborates the findings in Fig. 9(c), indicating a heterogeneous distribution of deformation resistance in Grain A under simple shear, whereas Grain B displays more uniform deformation resistance. Consequently, the analysis in Fig. 9(b) leads to the conclusion that CDRX predominantly occurs in the $(1\bar{2}1)[001]$-oriented Grain A, while GDRX develops in the (111)[110]-oriented Grain B. Thus, both GDRX and CDRX are actively engaged during the DRX acceleration phase in the hot-torsion processing of Al–7Mg.

According to Zhang and Wilson [46], subjecting a FCC polycrystalline material to simple shear would lead to the alignment of shear planes in the polycrystals, either parallel or perpendicular to the main shear plane (111). This prediction provides a plausible explanation for the observation that grains A and B in Fig. 9(b) display shear planes of $(1\bar{2}1)$ and (111), respectively, which are either perpendicular or parallel to the main shear plane (111). Given that sub-grain boundaries are oriented perpendicular to the shear direction, the [001] orientation in grain A indicates the formation of (001)-type sub-grain boundaries, as depicted in Fig. 9(b-ii). Similarly, it can be inferred that grain B primarily forms (110)-type sub-grain boundaries, aligning with the shear direction and possessing [110] orientation. These observations align with Winther's predictions [47], which state that the cross-slipping of dislocations onto the second neighboring slip plane leads to the formation of (001) sub-grain boundaries, while cross-slipping onto the first neighboring slip plane results in

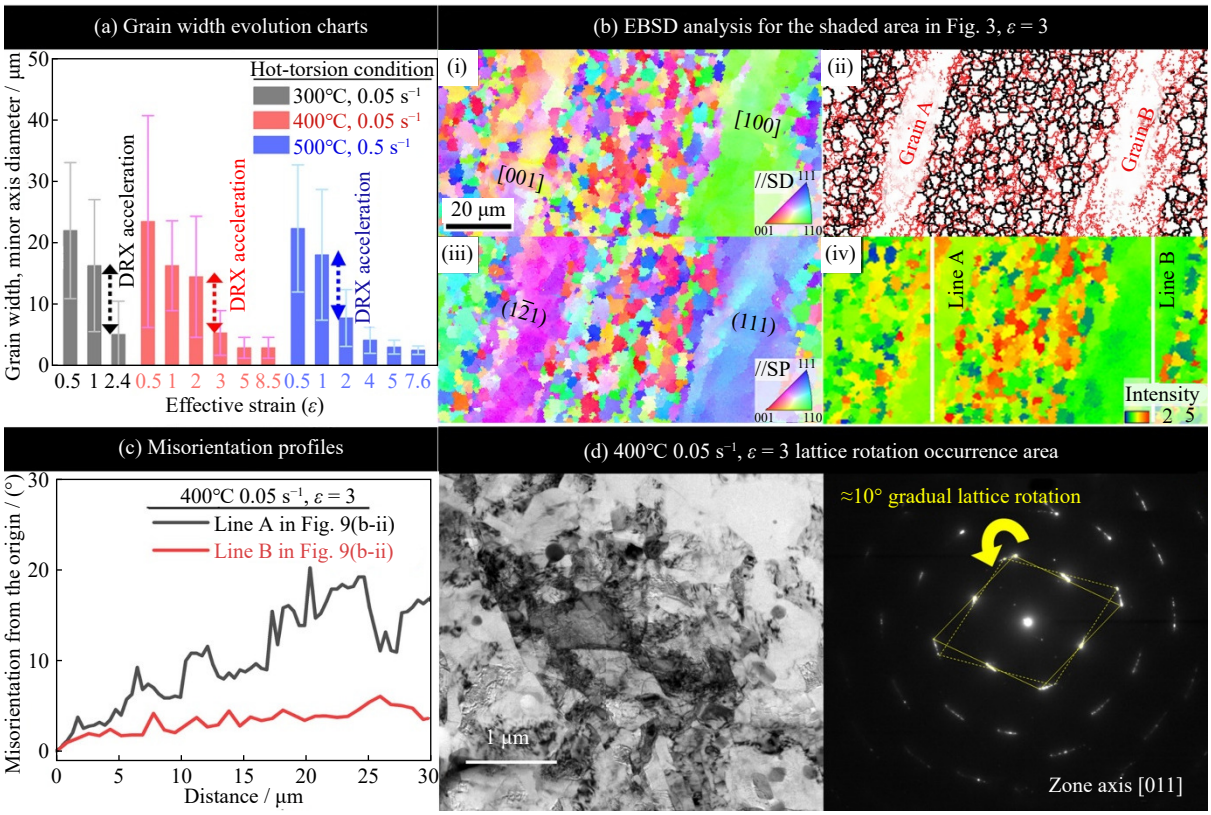

Fig. 9. (a) Grain width variation charts for the three deformation conditions during hot-torsion, (b) EBSD analyses conducted for the shaded area in Fig. 3 and $\varepsilon = 3$, including (i) IPF map displaying grain orientations corresponding to the shear direction, (ii) grain boundary map decorated with black lines ($\theta > 15°$) and red lines ($\theta < 15°$), (iii) IPF map displaying grain orientations corresponding to the shear plane, (iv) Taylor factor map calculated from a deformation gradient tensor for the torsion around the horizontal axis in the image, (c) misorientation profile from the origin along the two white lines in Fig. 9(b-iv), and (d) TEM observation for a lattice rotation occurrence area in the 400°C 0.05 s^{-1} $\varepsilon = 3$ sample.

(110) sub-grain boundaries. The greater slip plane rotation required (≈109.4°) for the former cross-slip, compared to the latter (≈70.5°), implies more lattice rotation about the [110] axis during CDRX formation in the $(1\bar{2}1)[001]$-oriented grain A. This hypothesis is partly supported by the TEM observation of a substructure in Fig. 9(d), showing clear evidence of a 10° lattice rotation about the [110] axis. However, this observation merely indicates the role of cross-slips in grain rotation or substructure formation and does not conclusively prove that larger cross-slips occur in the $(1\bar{2}1)[001]$-oriented grain compared to the (111)[110]-oriented grain. Thus, further research is required to elucidate the impact of cross-slip magnitude on the evolution of parent grain orientation during the hot deformation of FCC metals.

In other words, the data suggest that CDRX and GDRX play pivotal roles in the increase of XDRX following DRX acceleration. Grain A, with a $(1\bar{2}1)[001]$ orientation, predominantly undergoes CDRX, while grain B, with a (111)[110] orientation, experiences GDRX during the microstructural evolution. The orientation of these parent grains likely results from the gradual grain rotation induced by simple shear, as suggested by [46–47]. Additionally, the variance in their cross-slip systems is thought to contribute to these distinct grain orientations.

4.2. Texture index evolution during hot-torsion

Material anisotropy, quantified by the TI, is observed to decrease during the hot torsion of Al–7Mg alloys within the temperature range of 300 to 500°C, as depicted in Fig. 5. The TI values peak at $\varepsilon = 0.5$, mirroring the trend observed in the TI evolution of cold-rolled Al–Mg alloys [48], where increasing cold rolling reductions led to a gradual increase in TI. However, the absolute TI values reported in previous studies for rolling [48–49], equal channel angular pressing [50], and high-pressure torsion [51] ranged between 2 and 10 at various strains, significantly lower than the TI values of 15 to 27 observed at $\varepsilon = 0.5$ in Fig. 5. The elevated TI values at $\varepsilon = 0.5$ can be attributed to the hot extrusion process conducted prior to the hot torsion tests, as a hot-extruded Al alloy exhibited a relatively high TI value of 30 [52].

A critical observation from Fig. 5 is that over 70% of the TI reduction occurs up to a strain level of 2 within 300–500°C temperature range. This indicates that significant grain rotation occurs to diminish material anisotropy. However, as illustrated in Fig. 8, the increase in X_{DRX} varies from 0.03 to 0.25, depending on the temperature, suggesting that DRX is not the main contributor to the TI reduction. Alongside the flow curves in Fig. 1, which show flow softening at small strains (≤2), the evolution of lattice orientation distribution depicted in Fig. 3 reveals a gradual development of sub-grains within the larger parent grain from $\varepsilon = 0.5$ to $\varepsilon = 3$. Moreover, the simple shear applied during hot torsion leads to the formation of $(1\bar{2}1)[001]$- and (111)[110]-ori-

ented parent grains, as discussed in Section 4.1.2. This suggests that the observed reduction in TI is not predominantly due to the formation of mature DRX. Instead, the rotation of parent grains and the emergence of sub-grains are notably influential in reducing material anisotropy.

5. Conclusions

In this study, we investigated the progressive dynamic recrystallization (DRX) and texture behaviors during hot deformation in the Al–7Mg alloy. Hot-torsion tests were conducted at various temperatures (300, 400, and 500°C) and strain rates (0.05, 0.5, and 5 s^{-1}), and microstructure observations were performed to analyze the DRX and texture characteristics. The main conclusions drawn from the study are as follows:

(1) The measured DRXed grain fraction (X_{DRX}) plot suggests that the DRX behavior of the Al–7Mg alloy can be divided into two stages until the full DRX structure is achieved: Stage 1 involves a moderate increase in X_{DRX} (0.03–0.25) depending on the hot-torsion conditions. This increase mainly occurs at $\varepsilon \leq 0.5$ and remains relatively unchanged until the onset of the DRX acceleration stage. Stage 2, defined as the DRX acceleration stage, is characterized by a substantial increase in X_{DRX}, reaching ~0.9. The calculated DRX kinetics successfully predict the rate of DRX during this stage.

(2) In Stage 1, discontinuous DRX primarily dominates, while in Stage 2, continuous and geometric DRXs (CDRX and GDRX) are predominantly observed within $(1\bar{2}1)[001]$- and (111)[110]-oriented parent grains, respectively. Clear sub-grain structure formation was observed in the CDRXed $(1\bar{2}1)[001]$ grain, attributed to a larger rotation between slip planes compared to the GDRXed (111)[110] grain during hot-torsion.

(3) The overall improvement in texture randomness in the Al–7Mg alloy does not closely correlate with the increase in X_{DRX}. Instead, changes in texture randomness are primarily driven by the rotation of parent grains and the formation of sub-grains.

Acknowledgements

This work was partly supported by the National Research Foundation of Korea (NRF) grant funded by the Korea government (MSIT) (No. 2020R1C1C1005726), Technology development Program (No. RS-2023-00220823) funded by the Ministry of SMEs and Startups (MSS, Korea), the Electronics Technology Development Project (No. 20026289) funded By the Ministry of Trade, Industry & Energy (MOTIE, Korea), and partly supported by the research grant of the Kongju National University in 2022. The present authors greatly appreciate the material supply from the Korea Institute of Industrial Technology (KITECH) with the permission of Dr. Bong-Hwan Kim and Dr. Shae K. Kim, Principal researchers at KITECH.

Conflict of Interest

The authors declare that they have no known competing financial interests or personal relationships that could have appeared to influence the work reported in this paper.

References

[1] F.J. Humphreys and M. Hatherly, *Recrystallization and Related Annealing Phenomena*, Elsevier, Amsterdam, 2004.
[2] H.J. McQueen, S. Spigarelli, M.E. Kassner, and E. Evangelista, *Hot Deformation and Processing of Aluminum Alloys*, CRC Press, Boca Raton, 2016.
[3] J.J. Jonas, Dynamic recrystallization—Scientific curiosity or industrial tool?, *Mater. Sci. Eng. A*, 184(1994), No. 2, p. 155.
[4] N. Ravichandran and Y.V.R.K. Prasad, Dynamic recrystallization during hot deformation of aluminum: A study using processing maps, *Metall. Trans. A*, 22(1991), No. 10, p. 2339.
[5] L. Xing, P.F. Gao, M. Zhan, Z.P. Ren, and X.G. Fan, A micromechanics-based damage constitutive model considering microstructure for aluminum alloys, *Int. J. Plast.*, 157(2022), art. No. 103390.
[6] K. Huang and R.E. Logé, A review of dynamic recrystallization phenomena in metallic materials, *Mater. Des.*, 111(2016), p. 548.
[7] Y.C. Lin, X.H. Zhu, W.Y. Dong, H. Yang, Y.W. Xiao, and N. Kotkunde, Effects of deformation parameters and stress triaxiality on the fracture behaviors and microstructural evolution of an Al–Zn–Mg–Cu alloy, *J. Alloys Compd.*, 832(2020), art. No. 154988.
[8] L.E. Murr, *Interfacial Phenomena in Metal and Alloys*, Addison-Wesley Pub. Co., Boston, 1975.
[9] R.W. Hertzberg, R.P. Vinci, and J.L. Hertzberg, *Deformation and Fracture Mechanics of Engineering Materials*, John Wiley & Sons, Hoboken, 2020.
[10] E.I. Galindo-Nava, J. Sietsma, and P.E.J. Rivera-Díaz-del-Castillo, Dislocation annihilation in plastic deformation: II. Kocks–Mecking analysis, *Acta Mater.*, 60(2012), No. 6-7, p. 2615.
[11] E.I. Galindo-Nava and P.E.J. Rivera-Díaz-del-Castillo, Thermostatistical modelling of hot deformation in FCC metals, *Int. J. Plast.*, 47(2013), p. 202.
[12] W. Blum, Q. Zhu, R. Merkel, and H.J. McQueen, Geometric dynamic recrystallization in hot torsion of Al–5Mg–0.6Mn (AA5083), *Mater. Sci. Eng. A*, 205(1996), No. 1-2, p. 23.
[13] G.A. Henshall, M.E. Kassner, and H.J. McQueen, Dynamic restoration mechanisms in Al-5.8 At. Pct Mg deformed to large strains in the solute drag regime, *Metall. Trans. A*, 23(1992), No. 3, p. 881.
[14] H.W. Son, J.C. Lee, C.H. Cho, and S.K. Hyun, Effect of Mg content on the dislocation characteristics and discontinuous dynamic recrystallization during the hot deformation of Al–Mg alloy, *J. Alloys Compd.*, 887(2021), art. No. 161397.
[15] M. Zecevic, R.A. Lebensohn, R.J. McCabe, and M. Knezevic, Modelling recrystallization textures driven by intragranular fluctuations implemented in the viscoplastic self-consistent formulation, *Acta Mater.*, 164(2019), p. 530.
[16] O. Engler, Texture and anisotropy in the Al–Mg alloy AA 5005–Part I: Texture evolution during rolling and recrystallization, *Mater. Sci. Eng. A*, 618(2014), p. 654.
[17] S. Tamimi, G. Sivaswamy, I. Violatos, S. Moturu, S. Rahimi, and P. Blackwell, Modelling and experimentation of the evolution of texture in an Al–Mg alloy during earing cupping test, *Procedia Eng.*, 207(2017), p. 1.
[18] O. Engler and S. Kalz, Simulation of earing profiles from tex-

ture data by means of a visco-plastic self-consistent polycrystal plasticity approach, *Mater. Sci. Eng. A*, 373(2004), No. 1-2, p. 350.
[19] J. Wang, X.J. Zhang, X. Lu, Y.S. Yang, and Z.H. Wang, Microstructure, texture and mechanical properties of hot-rolled Mg–4Al–2Sn–0.5Y–0.4Nd alloy, *J. Magnesium Alloys*, 4(2016), No. 3, p. 207.
[20] K. Yoshida, Y. Tadano, and M. Kuroda, Improvement in formability of aluminum alloy sheet by enhancing geometrical hardening, *Comput. Mater. Sci.*, 46(2009), No. 2, p. 459.
[21] M. Rezayat, M.H. Parsa, H. Mirzadeh, and J.M. Cabrera, Texture development during hot deformation of Al/Mg alloy reinforced with ceramic particles, *J. Alloys Compd.*, 798(2019), p. 267.
[22] K. Yoshida, T. Ishizaka, M. Kuroda, and S. Ikawa, The effects of texture on formability of aluminum alloy sheets, *Acta Mater.*, 55(2007), No. 13, p. 4499.
[23] X. Zeng, X.G. Fan, H.W. Li, *et al*., Grain refinement in hot working of 2219 aluminium alloy: On the effect of deformation mode and loading path, *Mater. Sci. Eng. A*, 794(2020), art. No. 139905.
[24] I. Kovacs and P. Feltham, Determination of the work-hardening characteristics of metals at large strains by means of torsion, *Phys. Status Solidi B*, 3(1963), No. 12, p. 2379.
[25] H.W. Son, C.H. Cho, J.C. Lee, *et al*., Deformation banding and static recrystallization in high-strain-rate-torsioned Al–Mg alloy, *J. Alloys Compd.*, 814(2020), art. No. 152311.
[26] J.C. Li, X.D. Wu, L.F. Cao, B. Liao, Y.C. Wang, and Q. Liu, Hot deformation and dynamic recrystallization in Al–Mg–Si alloy, *Mater. Charact.*, 173(2021), art. No. 110976.
[27] K.T. Son, J.W. Lee, T.K. Jung, *et al*., Evaluation of dynamic recrystallization behaviors in hot-extruded AA5083 through hot torsion tests, *Met. Mater. Int.*, 23(2017), No. 1, p. 68.
[28] D. Odoh, Y. Mahmoodkhani, and M. Wells, Effect of alloy composition on hot deformation behavior of some Al–Mg–Si alloys, *Vacuum*, 149(2018), p. 248.
[29] G.J. Baxter, Q. Zhu, and C.M. Sellars, Effects of magnesium content on hot deformation and subsequent recrystallization behavior of aluminum–magnesium alloys, [in] *Proceedings of International Conference on Aluminum Alloys* (*ICAA*), 6(1998), p. 1233.
[30] H.T. Jeong, S.H. Han, and W.J. Kim, Effects of large amounts of Mg (5–13 wt%) on hot compressive deformation behavior and processing maps of Al–Mg alloys, *J. Alloys Compd.*, 788(2019), p. 1282.
[31] D.L. Sang, R.D. Fu, and Y.J. Li, The hot deformation activation energy of 7050 aluminum alloy under three different deformation modes, *Metals*, 6(2016), No. 3, art. No. 49.
[32] S.F. Medina and C.A. Hernandez, Modelling of the dynamic recrystallization of austenite in low alloy and microalloyed steels, *Acta Mater.*, 44(1996), No. 1, p. 165.
[33] V. Randle and O. Engler, *Introduction to Texture Analysis*: *Macrotexture*, *Microtexture and Orientation Mapping*, CRC Press, Boca Raton, 2000.
[34] S.I. Kim and Y.C. Yoo, Dynamic recrystallization behavior of AISI 304 stainless steel, *Mater. Sci. Eng. A*, 311(2001), No. 1-2, p. 108.
[35] S. Serajzadeh and A. Karimi Taheri, An investigation on the effect of carbon and silicon on flow behavior of steel, *Mater. Des.*, 23(2002), No. 3, p. 271.
[36] E.I. Poliak and J.J. Jonas, A one-parameter approach to determining the critical conditions for the initiation of dynamic recrystallization, *Acta Mater.*, 44(1996), No. 1, p. 127.
[37] J.J. Jonas, X. Quelennec. L. Jiang, and É Martin, The Avrami kinetics of dynamic recrystallization, *Acta Mater.*, 57(2009), No. 9, p. 2748.
[38] S. Gourdet and F. Montheillet, An experimental study of the recrystallization mechanism during hot deformation of aluminium, *Mater. Sci. Eng. A*, 283(2000), No. 1-2, p. 274.
[39] T. Sakai, H. Miura, A. Goloborodko, and O. Sitdikov, Continuous dynamic recrystallization during the transient severe deformation of aluminum alloy 7475, *Acta Mater.*, 57(2009), No. 1, p. 153.
[40] T. Sakai, A. Belyakov, R. Kaibyshev, H. Miura, and J.J. Jonas, Dynamic and post-dynamic recrystallization under hot, cold and severe plastic deformation conditions, *Prog. Mater. Sci.*, 60(2014), p. 130.
[41] H. Yamagata, Y. Ohuchida, N. Saito, and M. Otsuka, Nucleation of new grains during discontinuous dynamic recrystallization of 99.998 mass% aluminum at 453 K, *Scripta Mater.*, 45(2001), No. 9, p. 1055.
[42] R. Kapoor, G.B. Reddy, and A. Sarkar, Discontinuous dynamic recrystallization in α-Zr, *Mater. Sci. Eng. A*, 718(2018), p. 104.
[43] M. Mofarrehi, M. Javidani, and X.-G. Chen, Effect of Mn content on the hot deformation behavior and microstructure evolution of Al–Mg–Mn 5xxx alloys, *Mater. Sci. Eng. A*, 845(2022), art. No. 143217.
[44] A.G. Beer and M.R. Barnett, Microstructural development during hot working of Mg–3Al–1Zn, *Metall. Mater. Trans. A*, 38(2007), No. 8, p. 1856.
[45] A. Heidarzadeh, T. Saeid, V. Klemm, A. Chabok, and Y.T. Pei, Effect of stacking fault energy on the restoration mechanisms and mechanical properties of friction stir welded copper alloys, *Mater. Des.*, 162(2019), p. 185.
[46] Y. Zhang and C.J.L. Wilson, Lattice rotation in polycrystalline aggregates and single crystals with one slip system: A numerical and experimental approach, *J. Struct. Geol.*, 19(1997), No. 6, p. 875.
[47] G. Winther, Slip systems extracted from lattice rotations and dislocation structures, *Acta Mater.*, 56(2008), No. 9, p. 1919.
[48] S.Y. Li, P. Van Houtte, and S.R. Kalidindi, A quantitative evaluation of the deformation texture predictions for aluminium alloys from crystal plasticity finite element method, *Modell. Simul. Mater. Sci. Eng.*, 12(2004), No. 5, p. 845.
[49] O. Engler, E. Sachot, J.C. Ehrström, A. Reeves, and R. Shahani, Recrystallisation and texture in hot deformed aluminium alloy 7010 thick plates, *Mater. Sci. Technol.*, 12(1996), No. 9, p. 717.
[50] T. Khelfa, R. Lachhab, H. Azzeddine, *et al*., Effect of ECAP and subsequent annealing on microstructure, texture, and microhardness of an AA6060 aluminum alloy, *J. Mater. Eng. Perform.*, 31(2022), No. 4, p. 2606.
[51] S. Naghdy, L. Kestens, S. Hertelé, and P. Verleysen, Evolution of microstructure and texture in commercial pure aluminum subjected to high pressure torsion processing, *Mater. Charact.*, 120(2016), p. 285.
[52] Z. Chen, G.A. Sun, Y. Wu, *et al*., Multi-scale study of microstructure evolution in hot extruded nano-sized TiB_2 particle reinforced aluminum composites, *Mater. Des.*, 116(2017), p. 577.